Journal of Alloys and Compounds 580 (2013) 449–456

Contents lists available at SciVerse ScienceDirect

Journal of Alloys and Compounds

journal homepage: www.elsevier.com/locate/jalcom

Electromigration behaviors of $Ge_2Sb_2Te_5$ chalcogenide thin films under DC bias

Yin-Hsien Huang, Chi-Hang Hang, Yu-Jen Huang, Tsung-Eong Hsieh *

Department of Materials Science and Engineering, National Chiao Tung University, 1001 Ta-Hsueh Road, Hsinchu 30010, Taiwan, ROC

ARTICLE INFO

Article history:
Received 25 April 2013
Received in revised form 18 June 2013
Accepted 20 June 2013
Available online 29 June 2013

Keywords:
Chalcogenides
Electromigration
Black's theory
Blech structure
Phase-change random access memory

ABSTRACT

Electromigration (EM) behaviors of pristine $Ge_2Sb_2Te_5$ (GST), nitrogen-doped GST (N-GST) and cerium-doped GST (Ce-GST) thin-film strips under DC bias are presented. The mean-time-to-failure (*MTTF*) analysis based on the Black equation found that the EM failure times at room temperature are 1.2×10^4, 40 and 9.2×10^2 years and the activation energies (E_a) of EM process are 1.07, 0.57 and 0.68 eV for GST, N-GST and Ce-GST, respectively. Moreover, the calibration of the current density exponent, *n*, of Black's equation found *n* values are close to 2 for all samples, implying the dominance of grain boundary diffusion during the mass transport of EM process. For doped GSTs, the inferior EM failure lifespans and smaller E_a values were ascribed to the grain refinement effect which increases the number of grain boundaries in such samples. It consequently promoted the short-circuit diffusion and accelerated the EM failure in doped GSTs. The Blech-type tests on GSTs found that the threshold product, i.e., the product of current density and sample length ($(j \cdot L)_{th}$), is 200 A/cm for GST, 50 A/cm for N-GST and 66.67 A/cm for Ce-GST. Moreover, the product of diffusivity and effective charge number (i.e., DZ^*) for GST, N-GST and Ce-GST was 2.0×10^{-7}, 4.5×10^{-6} and 3.8×10^{-6} cm^2/sec, respectively. Analytical results illustrated that the electrostatic force effect dominates the EM failure in samples with short strip lengths while the electron-wind force effect dominates the EM failure in samples with long strip lengths. Doping might alleviate the mass segregation in GST; however, its effect was moderate.

© 2013 Elsevier B.V. All rights reserved.

1. Introduction

Nucleation-dominated chalcogenides, $Ge_2Sb_2Te_5$ (GST), is the most common programming material for phase-change random access memory (PRAM) due to its fast recrystallization rate, high-density storage capability, long cycleability, scalability, and compatibility with complementary metal–oxide–semiconductor (CMOS) technologies. Under the application of thermal or electrical power, GST could reversibly switch in between the amorphous and crystalline states and the corresponding change in reflectivity or electrical resistivity could be adopted for signal recording [1]. However, the heat generated during the switching process may degrade the chalcogenide layer [2–5]. The thermal stresses accompanied with the microstructure change of programming layer are the reliability concerns of PRAM due to the interfacial failures and compositional changes in GST [6–9]. In other words, electromigration (EM) is a crucial issue of PRAM failure.

Compositional change, electric-field-enhanced mass flow (i.e., the EM process) [2–4] and thermal diffusion [6] were suggested in the studies of PRAM failures. The driving forces of EM are commonly classified into two categories: the electrostatic force (i.e., direct force of the electrostatic field on the diffusing species) and the electron-wind force (i.e., momentum exchange between the moving charge carriers and the diffusing atoms) [10]. In the case of electrostatic force, the positively-charged ions tend to move in direction of the applied bias field and thus the mass accumulation is expected to occur at the cathode end of sample. On the other hand, the constituted elements move to the anode end of sample when electron-wind force effect dominates since the mass flows in the direction of the electron flow.

The mean-time-to-failure (*MTTF*) analysis based on the Black equation is widely adopted to evaluate the EM behaviors of samples subjected to electrical bias [11–13]. Black equation correlates the *MTTF* with current density (j) and activation energy (E_a) of EM process in a form of

$$MTTF = C'j^{-n} \exp\left(\frac{E_a}{kT}\right) \quad (1)$$

where C' is the geometrical constant, n is the accelerating factor, k is the Boltzmann's constant and T is the absolute temperature.

Blech developed the samples with specific geometry for analyzing the EM behaviors [14,15]. By studying the EM process of aluminum (Al) strips with various lengths deposited on TiN, Blech

* Corresponding author.
E-mail address: tehsieh@mail.nctu.edu.tw (T.-E. Hsieh).

0925-8388/$ - see front matter © 2013 Elsevier B.V. All rights reserved.
http://dx.doi.org/10.1016/j.jallcom.2013.06.129

observed that the chemical gradient resulted from mass accumulation and depletion at the strip ends would cause the EM threshold. The threshold current density was found to be inversely proportional to the strip length (L) and, accordingly, Blech derived the threshold product, $(j \cdot L)_{th}$, as

$$(j \cdot L)_{th} = \frac{\Delta\sigma\Omega}{eZ^{*}\rho} \tag{2}$$

where $\Delta\sigma$ is the normal stress difference between strip ends, Ω is the atomic volume, e is the electron charge, Z^* is the effective charge number of the ions and ρ is the resistivity. By knowing the value of $(j \cdot L)_{th}$ corresponding to a certain material type, one can predict the occurrence of EM failure in the sample with specific geometrical shape.

Alien-element doping is frequently adopted to modulate the physical properties of chalcogenides so that they may meet the requirements of PRAM applications [16–23]. For instance, doping may effectively improve the thermal stability and reduce the reset current of PRAM devices. However, the effects of doping on EM behaviors of chalcogenides are less reported. Further, several studies applied the pulsed electrical bias to chalcogenide lines and investigated the atom segregation in the samples at various crystalline states [24,25]. In these studies, the concept of hole wind force was proposed to elucidate the element redistribution in the samples. Lack of fundamental EM characteristics ignites this study to prepare the pristine GST, nitrogen-doped GST (N-GST) and cerium-doped GST (Ce-GST) samples in Black- and Blech-structure forms so as to investigate their EM behaviors under DC bias. For all samples, the E_a's of EM process were evaluated by the *MTTF* analysis with the aid of the Black's equation and the values of $(j \cdot L)_{th}$ were calibrated by examining the EM processes in the Blech structure samples. The evolutions of microstructure and composition in chalcogenide samples were also characterized and their correlations to the EM failure under DC bias are discussed as follows.

2. Experiments

The thin-film samples were prepared by using a sputtering system with background pressure better than 3×10^{-6} torr. The deposition of chalcogenide layers was carried out at the radio-frequency (RF) gun power of 55 W and working pressure of 3 mtorr with high-purity argon (Ar) as the inlet flow gas. The N-doping was achieved by adding the N_2 gas in the inlet Ar gas during sputtering at a N_2/Ar flow ratio of 2% (in the unit of sccm) [17]. The Ce doping was realized by the target-attachment sputtering method [18] in which the dopant content of GST was adjusted by the amounts of Ce foils mounted on the 3 in. GST target. For the *MTTF* test samples, 85-nm thick titanium (Ti) electrode pads with the distance of 150 μm apart were first deposited on thermally oxidized Si wafer substrates by the direct-current (DC) sputtering method in conjunction with the lift-off method. The 500-nm thick, dumbbell-shaped GST layers, either undoped or doped, were then formed on the Ti pads with the aid of photolithography process. After annealing at 300 °C for 1 h in Ar ambient to induce the recrystallization of GST phase, the samples were transferred to an *in situ* electrical property measurement system [17] in which the electric bias was supplied by a Keithley 2400 *I–V* sourcemeter. The EM tests at various temperatures (200, 225, 250, 275 and 300 °C) were then performed under appropriate current stress conditions. Note that the current densities for EM tests were adjusted in accord with the difference in resistivities of GST samples ($\rho_{GST} = 8.4 \times 10^{-3}\ \Omega$ cm; $\rho_{N\text{-}GST} = 5.4 \times 10^{-2}\ \Omega$ cm; $\rho_{Ce\text{-}GST} = 4.8 \times 10^{-2}\ \Omega$ cm) [17,18]. In this study, the current density for GST and N-GST samples was 3.2×10^5 A/cm^2 while that for Ce-GST sample was 2×10^4 A/cm^2. The resistance changes as a function of time were monitored until abrupt resistance increments occurred in samples.

For the preparation of Blech structure samples, TiN electrode pads were first deposited on Si substrates by reactive sputtering of Ti at the condition of DC gun power of 100 W, working pressure of 3 m torr and the N_2/Ar mixed inlet gas flow at a ratio of 20% (in the unit of sccm). Afterward, a series of chalcogenide strip samples, either undoped or doped, with a width of 5 μm, thickness of 150 nm and lengths ranging from 10 to 45 μm were deposited on TiN layers by RF sputtering at the condition delineated above. The EM tests of the Blech-structure samples subjected to the current stressing ranging from 3.33×10^4 to 5.33×10^5 A/cm^2 were similarly performed in the *in situ* electrical property measurement system at the temperature of 300 °C.

Transmission electron microscopy (TEM; JEOL JEM 2010) was adopted to characterize the microstructures of various GST samples. Evolution of sample morphology was examined by scanning electron microscopy (SEM; JEOL JEM 6500F). Element distributions along the line direction of GST samples prior and posterior to the EM tests were analyzed by line scan method within an energy dispersive spectrometer (EDS; OXFORD INSTRUMENTS INCA *x*-Sight MODEL 7557) attached to the SEM.

3. Results and discussion

Fig. 1a–c separately present the plan-view TEM (PTEM) micrographs of GST, N-GST and Ce-GST subjected to 300 °C/1 h annealing. All GST samples possess the polycrystalline structure while the doped GSTs possess fine grain sizes. The selected area electron diffraction (SAED) patterns attached at the upper right-hand corners of TEM micrographs indicate that all the samples are of the face-centered cubic structure.

Fig. 2a–c present the profiles of resistance change against the time at various temperatures for GST, N-GST and Ce-GST samples subjected to the *MTTF* test. In this work, we define the time corresponding to the abrupt resistance increment as the *MTTF* of sample proposed by previous work [26]. Fig. 2d plots the ln(*MTTF*) against $1/kT$ and it indicates that the *MTTF* times of doped GSTs are longer than that of pristine GST at the same temperature. We note that the *MTTF* tests are often performed at elevated temperatures under current stressing conditions so as to accelerate the EM failure. It is well known that the doping may effectively improves the thermal stability of GST [18–20] and, hence, the doped GSTs exhibit better *MTTF* time properties at the test temperatures of 200–300 °C. With the aid of Eq. (1) and the slopes of ln(*MTTF*) against $1/kT$ plots shown in Fig. 2d, the EM failure times at room temperature were found to be 1.2×10^4, 40 and 9.2×10^2 years for GST, N-GST and Ce-GST, respectively, as deduced by the linear regression method. This indicates that doping in fact accelerates the EM failure of GST under practical operating conditions. Moreover, the slopes of

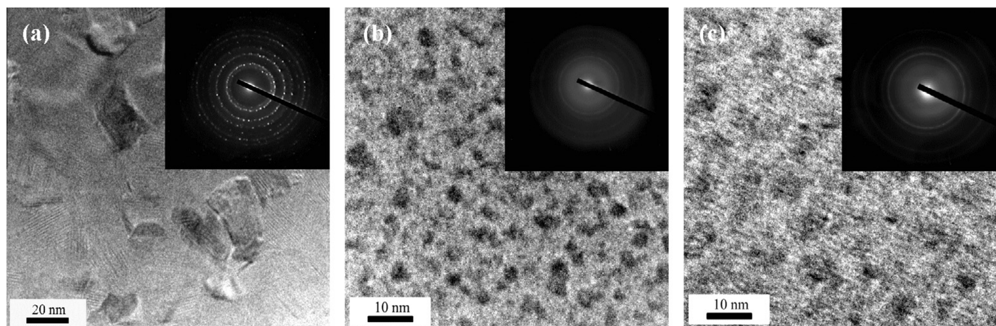

Fig. 1. PTEM micrographs of (a) GST, (b) N-GST and (c) Ce-GST samples subjected to annealing at 300 °C for 1 h. Corresponding SAED pattern is inserted at the right-hand corner of each micrograph.

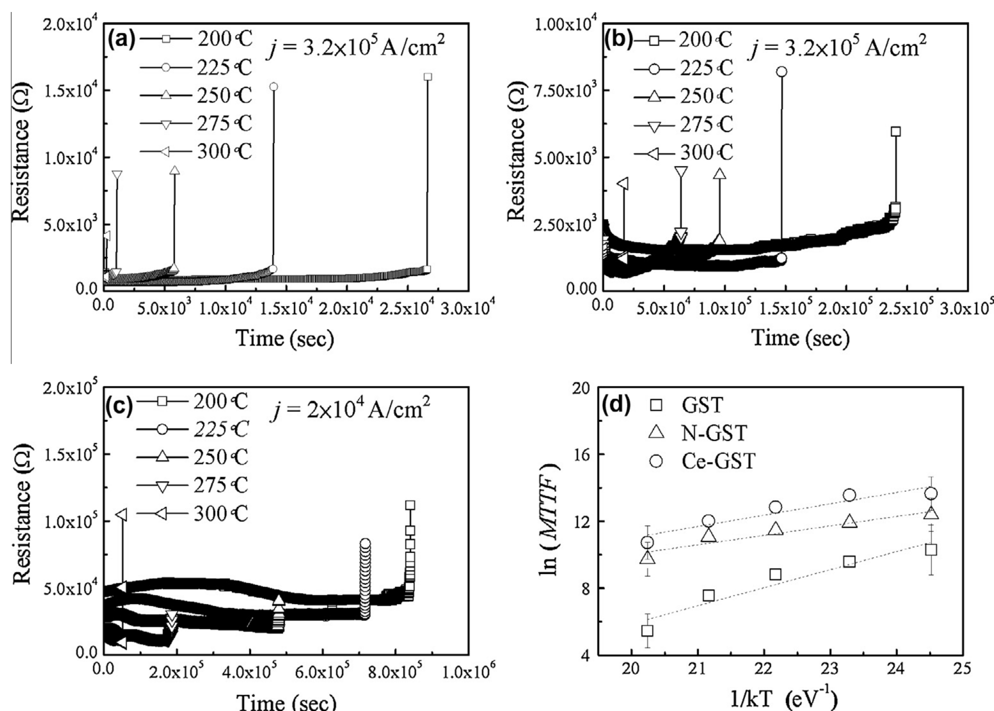

Fig. 2. Resistance change against time of (a) GST, (b) N-GST and (c) Ce-GST samples subjected to *MTTF* test at various temperatures. (d) shows the plots of ln(*MTTF*) against 1/*kT* for GST, Ce-GST and N-GST.

ln(*MTTF*) against $1/kT$ plots indicate that the E_a's of GST, N-GST and Ce-GST samples are 1.07, 0.56 and 0.68 eV, respectively. The decrement of E_a's in doped GSTs indicates doping in fact weakens the resistance to EM failure although it is well known for the thermal stability improvement of chalcogenides and the reduction of power consumption of PRAM devices [16–23].

In order to examine the heating effects on sample failure, a preliminary experiment by heating the GST, N-GST and Ce-GST *MTTF* test samples at 200 °C for 240 h (=8.64×10^6 s) in vacuum without applying the electrical bias was performed. As shown by the SEM micrographs and EDS line scan profiles in Fig. 3a and b, all samples remain intact without obvious element loss. Notably, GST is eutectic alloy featured by covalent bonding and the result of Fig. 3 is in agreement with that of the differential scanning calorimetry analysis performed by Yamada et al. [27] who reported no phase separation in GST at temperatures up to its melting point (T_m = 593 °C). As mentioned previously, we have adjusted the current densities applied to the samples in order to avoid the resistivity heating effect. For instance, the current density of 3.2×10^5 A/cm^2 resulted in an about 3.3 °C temperature increment in the sample subjected to *MTTF* test as revealed by the measurement of the temperature coefficient of resistance (TCR) of samples. This is negligibly small in comparison with the temperatures of our *MTTF* test at 200–300 °C. Analytical results presented above clearly indicate that the stoichiometry of GST samples remain stable before the occurrence of EM failure and the resistivity heating is not the primary cause of failure as depicted by Fig. 2a–c. Resistivity heating effect might emerge in the late stage of EM process when the mass depletion at cathode side substantially reduced the cross-sectional area of sample. It resulted in the increase of sample resistance and the local heating consequently aggravated the EM failure. We note that the increase of sample resistance can be clearly seen in Fig. 2a–c, in particular, in the time duration before the occurrence of abrupt resistance change in the samples.

Fig. 4a–c present the resistance profiles against the time at various current densities for chalcogenide samples subjected to the *MTTF* test at 200 °C. Fig. 4d plots the ln(*MTTF*) against ln(j) in terms of the data presented in Fig. 4a–c. With the aid of Eq. (1), the slopes of the plots allow the calibration of the current density exponent, n, of Black's equation and n of 1.98 for GST, 1.96 for N-GST and 1.80 for Ce-GST are separately identified. Shatzkes and Lloyd employed the theoretical model based on the vacancy diffusion and void nucleation processes for elucidating the physical significances involved in the n value of Black's equation [28]. Their analysis indicated that the n value of 2 implies the dominance of grain boundary diffusion during the EM process. Moreover, grain boundary diffusion might be the dominant mass transport process when the temperature is less than $0.6T_m$ of the sample [29]. The temperature of our *MTTF* test at 200 °C is about $0.55T_m$ of GST and, in conjunction with the n values delineated above, we hence infer that grain boundary diffusion plays an essential role in the EM failure of GST samples subjected to the *MTTF* test. As to the lower E_a values for doped GST samples presented in Fig. 2d, it is ascribed to the grain refinement effect that increases the number of grain boundaries and amplifies the short-circuit diffusion in such samples.

Fig. 5a presents the SEM micrographs of GST sample prior to the *MTTF* test and Fig. 5b–d depict the failed GST samples subjected to the *MTTF* test at 200 °C. As shown in Fig. 5b–d, the preferential failure occurring at the cathode sides of samples indicates the failure is correlated to the EM process. Voids tended to form at the cathode side as the mass kept on moving from cathode to anode side due to the electron-wind force effect. The gradual depletion of mass resulted in the increase of local current density at cathode side and, hence, the EM failure.

Fig. 6a–d present the EDS line scan profiles along the line direction of GST samples prior to and subjected to the *MTTF* test with $j = 3.2 \times 10^5$ A/cm^2 at 200 °C for 5 h. The EM-induced element segregation can be readily seen, i.e., Ge and Sb segregate toward the cathode side while Te segregates toward the anode side in the samples, a result similar to that reported by Yang et al. [2,3]. Nevertheless, the EM theory indicates the dominance of electron-wind force should drive all elements to the anode side. Such a discrepancy can

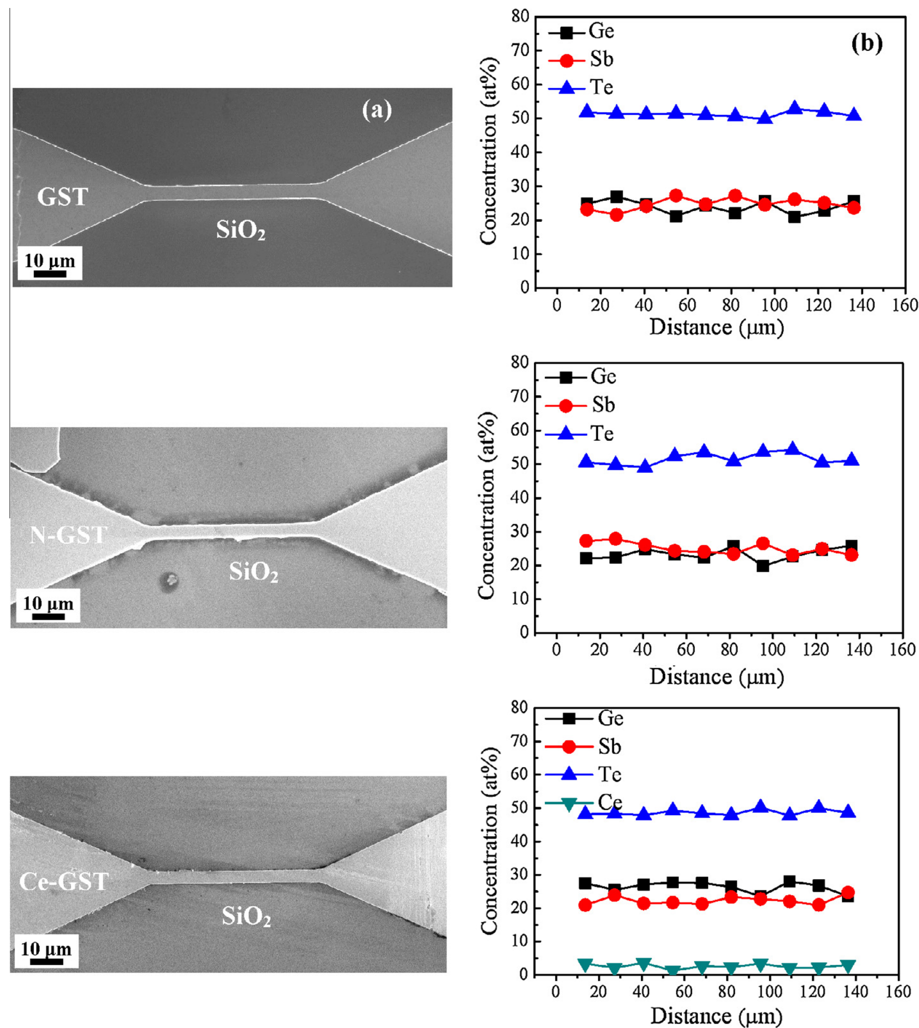

Fig. 3. (a) SEM micrographs and (b) EDS line scanning profiles for various *MTTF* test samples subjected to the heating at 200 °C for 240 h (=8.64 × 10^6 s) in vacuum without applying electrical bias.

be explained by the difference in element migration rates and the relative feature of composition data deduced by EDS analysis. Among the elements involved in GST, Te has been reported to possess the highest mobility under the action of electrical force [24]. The relatively fast depletion of Te in anode side would then cause the enrichment of Ge and Sb in cathode side as the EDS delineates the composition change in relative manner. This implies the impression that the elements in GST samples seem to segregate in different directions of bias field. In Ce-GST, the segregation directions of Te and Ge are the same as those in GST and N-GST whereas Sb exhibits a fluctuated distribution without preferential segregation trend. A comparison of the severity of element segregation depicted in Fig. 6a–d indicates that doping may alleviate the element segregation in GSTs only in a moderate manner. This is similarly ascribed to the increase of grain boundaries in doped GST samples which amplifies the short-circuit diffusion. It neutralized the blocking effects of dopants and, hence, was unable to suppress the EM-induced element segregation in doped GSTs in an obvious manner.

Fig. 7 shows a representative SEM micrograph of Blech-structure GST strips prior and posterior to the current stressing at 300 °C for 12 h. The threshold phenomenon predicted by Blech's theory was observed in such samples. According to the stressing current densities and the critical strip lengths of samples as delineated by the rectangles in Fig. 7, the values of $(j \cdot L)_{th}$ were found to be 200 A/cm for GST (L = 30 μm at j = 6.67 × 10^4 A/cm^2), 50 A/cm for N-GST (L = 15 μm at j = 3.33 × 10^4 A/cm^2) and 66.7 A/cm for Ce-GST (L = 20 μm at j = 3.33 × 10^4 A/cm^2). This indicates that, at a fixed j value, the critical length of doped GST is less than that of pristine GST. The smaller $(j \cdot L)_{th}$ values for doped GSTs imply the degradation of EM resistance by doping [30,31], a result similar to that observed in the *MTTF* test. It is noted that in this study the lengths of *MTTF* samples (L = 150 μm) are longer than those of Blech-structure strips ($L \leqslant 45$ μm). The $j \cdot L$ value for GST and N-GST is 4800 A/cm and that for Ce-GST is 300 A/cm for *MTTF* samples, which are much greater than the $(j \cdot L)_{th}$ values of Blech-structure samples. The electron-wind effect hence dominated the failure of *MTTF* samples as presented in Fig. 5 since the chemical composition gradient opposite to the electron-wind effect is comparatively weak in such samples.

In contrast to the *MTTF* test results, the mass depletion at anode side became rather obvious in the Blech-structure strips with relatively short lengths. Such a mass segregation phenomenon is evidenced by the enlarged SEM micrographs of Fig. 8a–c which depict the morphologies of the GST strips with L = 35 μm subjected to various stressing current densities and times at 300 °C. Note that the critical current density for the 35 μm GST, N-GST and Ce-GST Blech-structure strips is separately equal to 5.7 × 10^4 A/cm^2, 1.4 × 10^4 A/cm^2 and 1.9 × 10^4 A/cm^2 according to the $(j \cdot L)_{th}$ values delineated above. For the Blech-structure strips subjected

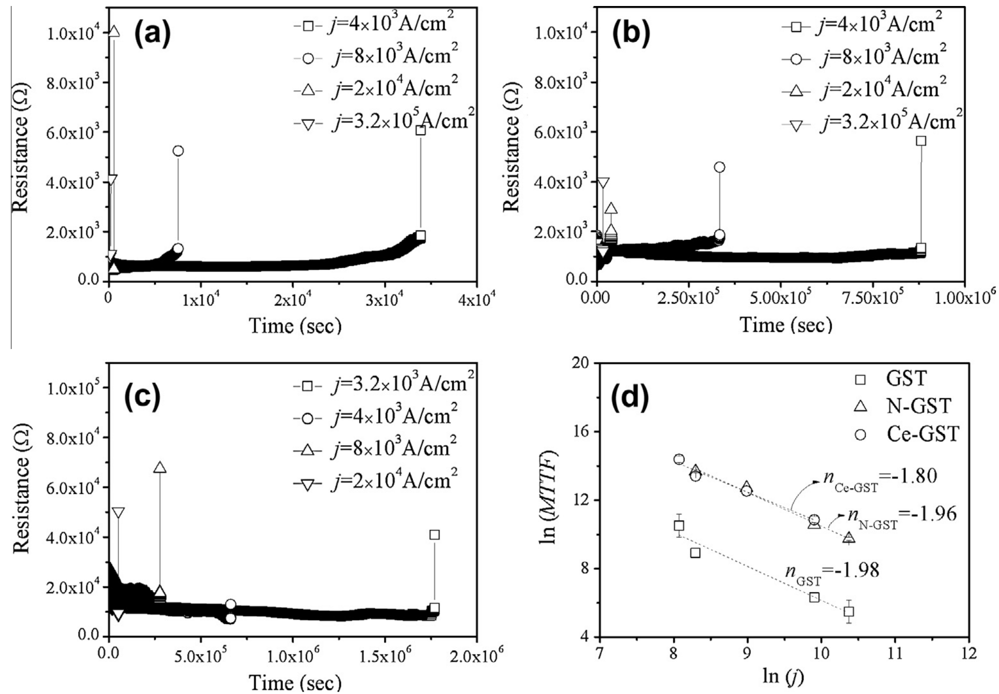

Fig. 4. Resistance change against time of (a) GST, (b) N-GST and (c) Ce-GST samples subjected to *MTTF* test at various current densities at 200 °C. (d) is the data fitting analysis of density exponent, *n*, of Black's equation.

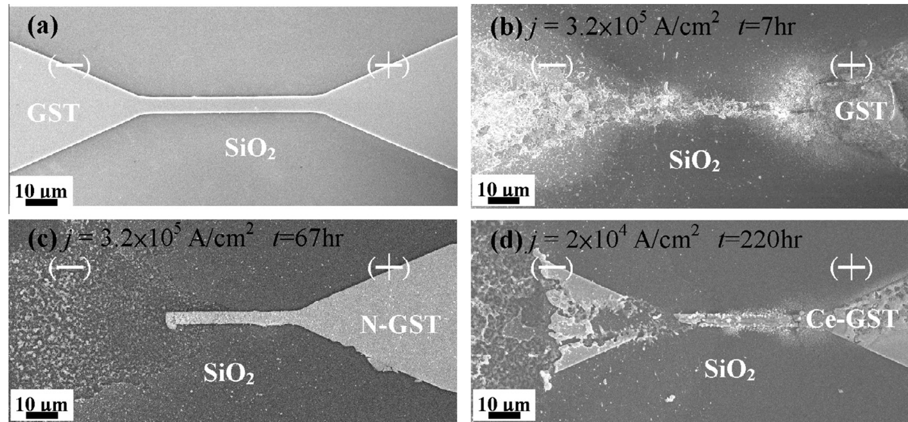

Fig. 5. SEM micrographs of (a) as-prepared GST sample and the failed (b) GST, (c) N-GST and (d) Ce-GST samples subjected to the *MTTF* test at 200 °C.

to the current stressing beyond the critical values, mass depletion at anode side can be readily seen and such an EM failure becomes pronounced with the increase of stressing current density. For the Blech-structure samples, the strips with short lengths resulted in strong chemical composition gradient to suppress the electron-wind effect and, hence, the mass depletion at cathode side as seen in *MTTF* samples was less obvious in such samples. As a matter of fact, the electron-wind-induced EM failure would be fully suppressed in Blech-structure sample when its length was below the critical value as illustrated in Fig. 8 [14,15]. The mass depletion at anode sides of Blech-structure samples with strip lengths greater than the critical values as depicted by Fig. 8a–c is hence ascribed to the electrostatic force effect.

Fig. 8a–c also depict a more severe void clustering in doped GST samples. As mentioned above, grain refinement increases the number of grain boundary in doped GSTs. In addition to providing the short-circuit diffusion, grain boundaries might also promote the void clustering since they are well-known heterogeneous nucleation sites. They might also serve as the defect sinks to release the stresses in doped GSTs induced by the difference in atomic sizes of dopants and elements of GST [32]. With the progress of void clustering, cross-sectional areas of doped GSTs reduced in a rate faster than that of pristine GST. This enhanced the local joule heating and the non-uniformity of current density, consequently amplifying the atomic flux divergence and shortens the EM lifespans of doped GSTs.

The EDS line scan profiles corresponding to GST, N-GST and Ce-GST Blech-structure strips subjected to the current stressing of 3.33×10^5 A/cm^2 in Fig. 8a–c are separately presented in Fig. 8d–f. It can be seen that the GST and N-GST exhibit a relatively uniform element distribution whereas moderate element segregation is observed in Ce-GST. Notably, EDS analysis on Blech-structure strips found their composition fluctuations are less obvious in comparison with the *MTTF* samples. This was probably caused by the dominance of electrostatic force in the relatively short Blech-structure strips and the magnitude of electrostatic force is known to be smaller

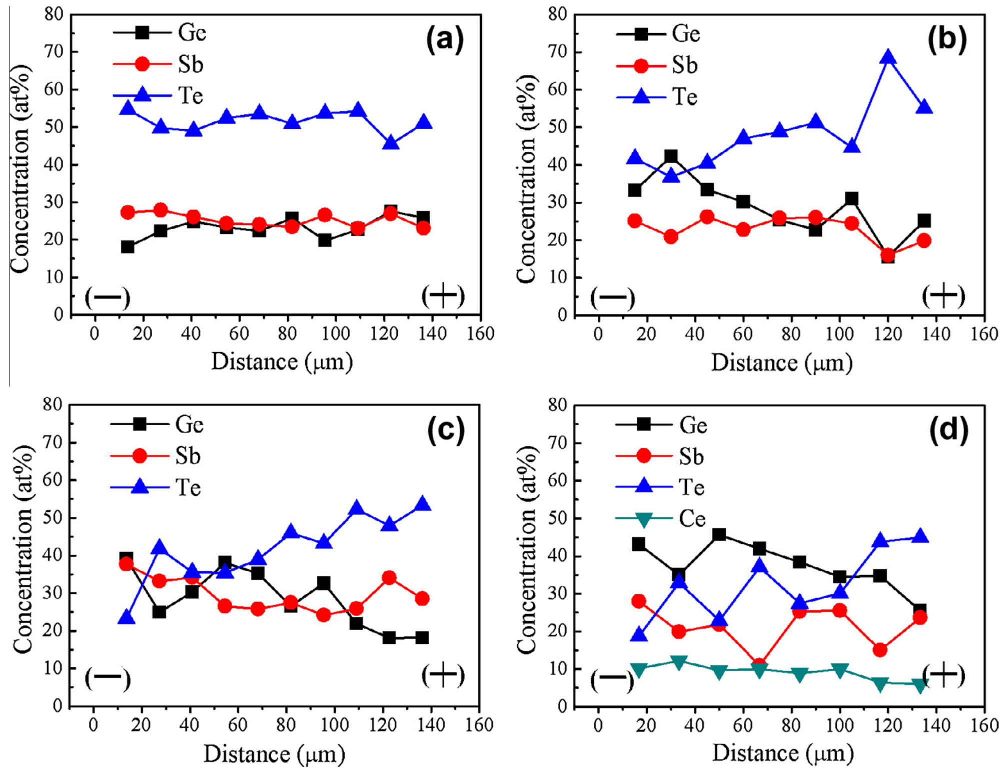

Fig. 6. EDS line scan profiles for (a) GST prior to the EM test, (b) GST, (c) N-GST and (d) Ce-GST samples subjected to the *MTTF* test with $j = 3.2 \times 10^5$ A/cm^2 at 200 °C for 5 h.

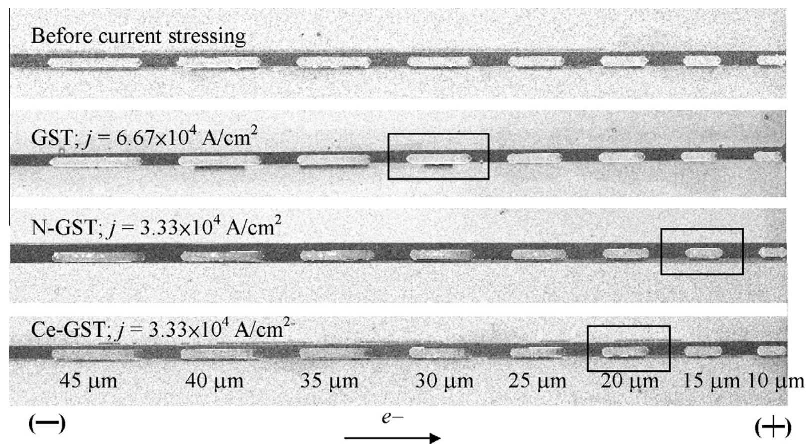

Fig. 7. A representative SEM micrograph of Blech-structure GST strips prior and posterior to the current stressing at 300 °C for 12 h. The strips with critical lengths are delineated by the rectangles.

than that of electron-wind force [10,33]. In Ce-GST strip with moderate element segregation, Ge tends to accumulate at the cathode side while Sb and Te segregate toward the anode side as depicted by Fig. 8f. Yang et al. pointed out that Te segregates toward the anode side regardless of the bias field direction and Ge and Sb move toward the cathode side when electrostatic force is the dominant EM mechanism [24]. The Ge and Te segregations are in agreement with the proposal of Yang et al., supporting the presence of electrostatic force in Blech-structure strips. Nevertheless, ambiguity arises in Sb as it segregates in the direction same as Te. We note that the EDS profiles presented in Fig. 8d–f are extracted from the Blech-structure strips with pronounced EM failure. The analytical results might not be accurate enough, in particular, in the regimes with severe mass depletion. As a result, the Sb segregation might requires a further study in order to clarify whether it is caused by the divergence of composition analysis or indeed an evidence of electrostatic effect as Sb segregates in the direction opposite to that observed in *MTTF* samples dominated by the electron-wind effect.

Huntington and Grone [10] derived the expression of average drift velocity (v) of atoms due to the EM process as:

$$v = \frac{DZ^{*} e \rho j}{kT} \tag{3}$$

where D is the diffusivity. The value of DZ^* or, the average migrating rate of effective charge under an electric bias, is commonly adopted to depict the EM rate which can be determined by the plot of v versus j. It is known that the average value of v for atoms in the strip samples can be obtained by dividing the depletion length with the stressing time. Fig. 9 plots the v versus j at 300 °C and the linear

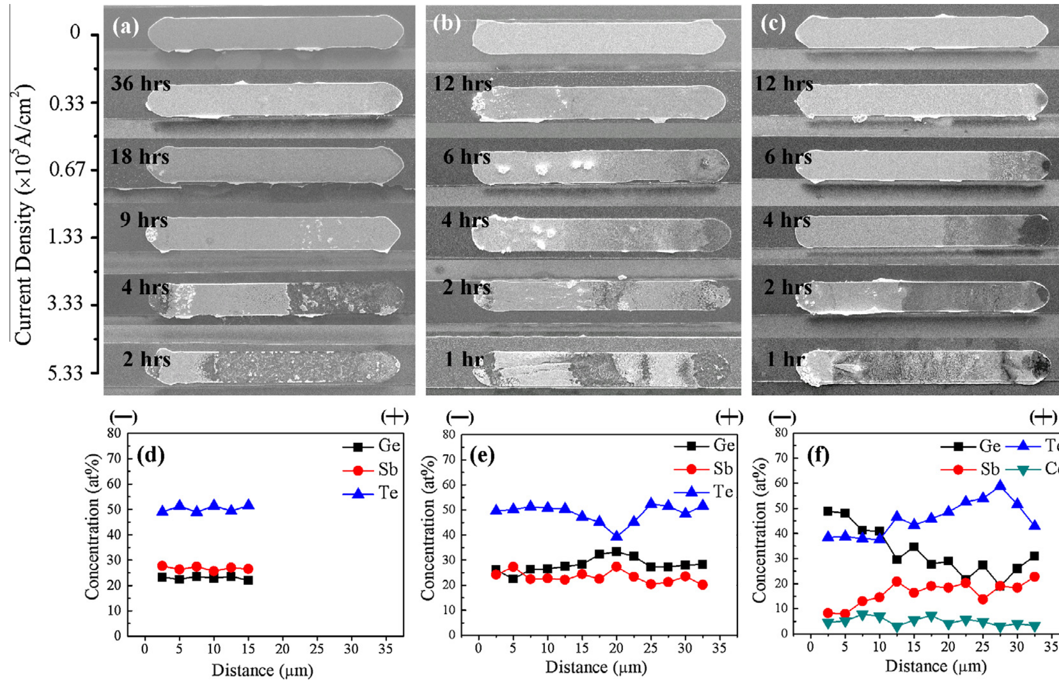

Fig. 8. Morphology evolutions of Blech-structure samples (a) GST, (b) N-GST, and (c) Ce-GST with $L = 35$ μm subjected to various stressing current densities at 300 °C. Note that the critical current density for 35 μm GST, N-GST and Ce-GST strips is separately equal to 5.7×10^4 A/cm^2, 1.4×10^4 A/cm^2 and 1.9×10^4 A/cm^2. (d–f) are the EDS line scan profiles corresponding to the Blech-structure samples in (a–c) with the stressing current density of 3.33×10^5 A/cm^2.

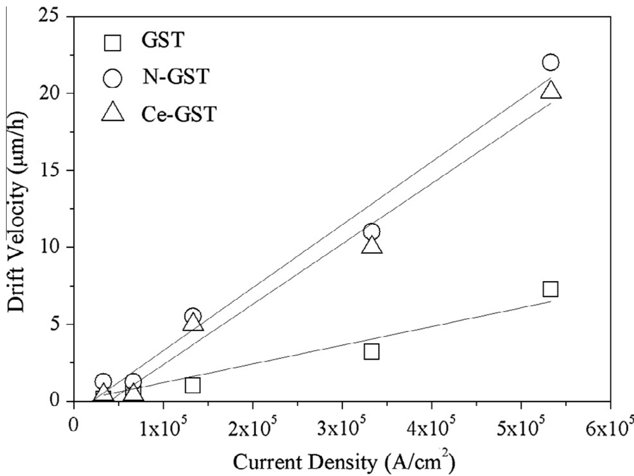

Fig. 9. Average drift velocity as a function of current density for GST, N-GST and Ce-GST strip samples at 300 °C.

relationship for the three GST samples can be seen. The extrapolation of the straight line to the $v = 0$ corresponds to the critical current density (j_c) and it allows us to find that the j_c is separately equal to 4.50×10^4 A/cm^2 for GST, 1.96×10^4 A/cm^2 for N-GST and 3.46×10^4 A/cm^2 for Ce-GST. Moreover, the DZ^* products for GST, N-GST and Ce-GST were found to be 2.0×10^{-7}, 4.5×10^{-6} and 3.8×10^{-6} cm^2/sec, respectively. The DZ^* values of doped GSTs are about 20 times higher than that of pristine GST, indicating doping accelerates the element migration in GST during EM process. This might be similarly ascribed to the grain refinement effect in doped GSTs which, in turn, amplifies the short-circuit diffusion of elements. Table 1 summarizes the key parameters calculated in terms of the analytical results of Blech-type test performed in this study. It should benefit the understanding on the element transport behaviors of chalcogenides subjected to the EM test under DC bias.

Table 1
A list of key EM parameters of GST, N-GST and Ce-GST samples calculated in terms of Blech-structure sample test.

Sample	ρ (10^{-2} Ω cm)[a]	j_c (10^4 A/cm^2)	$(j \cdot L)_{th}$ (A/cm)	DZ^* (10^{-6} cm^2/sec)
GST	0.84	4.50	200	0.2
N-GST	5.4	1.96	50	4.5
Ce-GST	4.8	3.46	66.67	3.8

[a] Measured at 300 °C.

4. Conclusions

This study presents the EM behaviors of pure GST and doped GSTs under DC bias. With the aid of Black's formula, the *MTTF* analysis of samples identified the current density exponent, n, is 1.98, 1.96 and 1.80 for GST, N-GST and Ce-GST, respectively. The n values are about equal to 2 for all GST samples, indicating the dominance of grain boundary diffusion during the mass transport of EM process in GSTs according to the study of Shatzkes and Lloyd [27]. Moreover, the values of E_a of EM process are 1.07, 0.56 and 0.68 eV for GST, N-GST and Ce-GST, respectively. The decrease of E_a's in doped GSTs was ascribed to the increase of grain boundaries due to the grain refinement effect which amplifies the short-circuit diffusion and consequently accelerates the EM failure. SEM/EDS analysis revealed that doping may alleviate the element segregation in GSTs; however, its effects are moderate.

The Blech-structure samples were also prepared to evaluate the EM behaviors of chalcogenides. Analytical results yielded the threshold products, $(j \cdot L)_{th}$ are separately equal to 200, 50, and 66.67 A/cm and the DZ^* values are 2.0×10^{-7}, 4.5×10^{-6} and 3.8×10^{-6} cm^2/sec for GST, N-GST and Ce-GST, respectively. The key EM parameters deduced by the Blech-type test similarly revealed the degradation of EM resistance in doped GSTs. Analytical results also illustrated that the electrostatic force effect dominates the EM failure in the samples with short strip lengths while the

electron-wind force effect dominates the EM failure in the samples with long strip lengths.

Acknowledgments

This work is supported by the National Science Council (NSC), Taiwan, ROC, under the contract No. NSC100-2221-E009-055-MY3.

References

[1] S.R. Ovshinsky, Phys. Rev. Lett. 21 (1968) 1450–1453.
[2] T.Y. Yang, I.M. Park, H.Y. You, S.H. Oh, K.W. Yi, Y.C. Joo, J. Electrochem. Soc. 156 (2009) H617–H620.
[3] T.Y. Yang, J.Y. Cho, Y.C. Joo, Electrochem. Solid-State Lett. 13 (2010) H321–H323.
[4] S.W. Nam, D. Lee, M.H. Kwon, D. Kang, C. Kim, T.Y. Lee, S. Heo, Y.W. Park, K. Lim, H.S. Lee, J.S. Wi, K.W. Yi, Y. Khang, K.B. Kim, Electrochem. Solid-State Lett. 12 (2009) H155–H159.
[5] C. Kim, D. Kang, T.Y. Lee, K.H.P. Kim, Y.S. Kang, J. Lee, S.W. Nam, K.B. Kim, Y. Khang, Appl. Phys. Lett. 94 (2009) 193504.
[6] J.-B. Park, G.-S. Park, H.-S. Baik, J.-H. Lee, H. Jeong, K. Kim, J. Electrochem. Soc. 154 (2007) H139–H141.
[7] S.O. Ryu, S.M. Yoon, K.J. Choi, N.Y. Lee, Y.S. Park, S.Y. Lee, B.G. Yu, J.B. Park, W.C. Shin, J. Electrochem. Soc. 153 (2006) G234–G237.
[8] S.-M. Yoon, K.-J. Choi, N.-Y. Lee, S.-Y. Lee, Y.-S. Park, B.-G. Yu, Appl. Surf. Sci. 254 (2007) 316–320.
[9] L. Zhang, X.-D. Han, Z. Zhang, J. Alloys Comp. 537 (2012) 71–75.
[10] H.B. Huntington, A.R. Grone, J. Phys. Chem. Solids 20 (1961) 76–87.
[11] J.R. Black, IEEE Trans. Electron. Dev. 16 (4) (1969) 338–347.
[12] J.R. Black, Proc. IEEE 57 (9) (1969) 1587–1594.
[13] M.Y. Hsieh, H.B. Huntington, J. Phys. Chem. Solids 39 (1978) 867–871.
[14] I.A. Blech, J. Appl. Phys. 47 (1976) 1203–1208.
[15] I.A. Blech, C. Herring, Appl. Phys. Lett. 29 (1976) 131–133.
[16] R. Kojima, S. Okabayashi, T. Kashihara, K. Horai, T. Matsunaga, E. Ohno, N. Yamada, T. Ohta, Jpn. J. Appl. Phys. 37 (1998) 2098–2103.
[17] Y.-J. Huang, Y.-C. Chen, T.-E. Hsieh, J. Appl. Phys. 106 (2009) 034916.
[18] Y.-J. Huang, M.-C. Tsai, C.-H. Wang, T.-E. Hsieh, Thin Solid Films 520 (2012) 3692–3696.
[19] S. Privitera, E. Rimini, C. Bongiorno, A. Pirovano, R. Bez, Nucl. Inst. Meth. Phys. Res. B 257 (2007) 352–354.
[20] J. Fu, X. Shen, Q. Nie, G. Wang, L. Wu, S. Dai, T. Xu, R.P. Wang, Appl. Surf. Sci. 264 (2013) 269–272.
[21] K. Do, H. Sohn, D.-H. Ko, J. Electrochem. Soc. 154 (2007) H867–H870.
[22] Y.-F. Hu, M.-C. Sun, S.-N. Song, Z.-T. Song, J.-W. Zhai, J. Alloys Comp. 551 (2013) 551–555.
[23] M. Zhu, L.-C. Wu, F. Rao, Z.-T. Song, X.-L. Li, C. Peng, X.-L. Zhou, K. Ren, D.-N. Yao, S.-L. Feng, J. Alloys Comp. 509 (2011) 10105–10109.
[24] T.-Y. Yang, I.-M. Park, B.-J. Kim, Y.-C. Joo, Appl. Phys. Lett. 95 (2009) 032104.
[25] S.-W. Nam, H.-S. Chung, Y.C. Lo, L. Qi, J. Li, Ye Lu, A.T. Charlie Johnson, Y. Jung, P. Nukala, R. Agarwal, Science 336 (2012) 1561–1566.
[26] W.J. Choi, E.C.C. Yeh, K.N. Tu, J. Appl. Phys. 94 (2003) 5665–5671.
[27] N. Yamada, E. Ohno, K. Nishiuchi, N. Akahira, M. Takao, J. Appl. Phys. 69 (1991) 2849–5856.
[28] M. Shatzkes, J.R. Lloyd, J. Appl. Phys. 59 (1986) 3890–3893.
[29] I. Kaur, Y. Mishin, W. Gust, Fundamentals of Grain and Interphase Boundary Diffusion, third ed., John Wiley, Chichester, 1995.
[30] J.E. Sanchez, L.T. McKnelly, J.W. Morris, J. Appl. Phys. 72 (1992) 3201–3203.
[31] E. Arzt, O. Kraft, W.D. Nix, J.E. Sanchez, J. Appl. Phys. 76 (1994) 1563–1571.
[32] B.N. Agarwala, G. Digiacomo, R.R. Joseph, Thin Solid Films 34 (1976) 165–169.
[33] K.-N. Tu, Solder Joint Technology: Materials, Properties, and Reliability, first ed., Springer, New York, 2007. pp. 211–243.